Analysis of Carrier Transport in Tunnel-Junction Vertical-Cavity Surface-Emitting Lasers by a Coupled Nonequilibrium Green's Function–Drift-Diffusion Approach

Alberto Tibaldi,[1,2,*] Jesús A. Gonzalez Montoya,[1] Matteo G. C. Alasio,[1] Alberto Gullino,[1] Anders Larsson,[3] Pierluigi Debernardi,[2] Michele Goano,[1,2] Marco Vallone,[1] Giovanni Ghione,[1] Enrico Bellotti,[4] and Francesco Bertazzi[1,2]

[1] *Department of Electronics and Telecommunications, Politecnico di Torino, Turin 10129, Italy*

[2] *Consiglio Nazionale delle Ricerche (CNR), Istituto di Elettronica e di Ingegneria dell'Informazione e delle Telecomunicazioni (IEIIT), Turin 10129, Italy*

[3] *Department of Microtechnology and Nanoscience, Chalmers University of Technology, Göteborg SE-412 96, Sweden*

[4] *Department of Electrical and Computer Engineering, Boston University, Boston, Massachusetts 02215, USA*

(Received 6 April 2020; revised 26 June 2020; accepted 16 July 2020; published 14 August 2020)

This work investigates carrier transport in tunnel junctions for vertical-cavity surface-emitting lasers (VCSELs). The study is performed with a quantum-corrected semiclassical approach, where tunneling is described rigorously with a nonequilibrium Green's function formalism based on a multiband description of the electronic structure. Validated with experimental results, the proposed approach provides a quantum-kinetic perspective of the tunneling process and paves the way toward a comprehensive theory of VCSELs, bridging the gap between semiclassical and quantum simulations.

DOI: 10.1103/PhysRevApplied.14.024037

I. INTRODUCTION

Tunnel junctions (TJs) are essential components in electronic and optoelectronic devices, such as multijunction solar cells [1,2], high-performance field-effect transistors [3], and light-emitting diodes [4]. TJs have been proposed for vertical-cavity surface-emitting lasers (VCSELs) to simultaneously provide hole injection and current confinement to the active region, with reduced series resistance and optical absorption [5]. Moreover, the critical wet-oxidation process needed to form the current aperture could be replaced with more reliable selective etching [6,7] or wafer-fusion processes [8–10]. Nevertheless, the present time-to-market is not compatible with the design from scratch of a revolutionized VCSEL architecture, which would require an extended campaign of wafer prototypes (each of them requiring several months and thousands of U.S. dollars). In this view, computer-aided design appears as the only viable instrument to trace the road map for the next generation of VCSELs.

Nanostructures are frequently embedded in tunneling elements of optoelectronic devices to address electrical-injection issues related to doping limitations and improve light extraction. For example, insertion of staggered-gap quantum wells (QWs) in GaAs TJs increases the peak tunneling current, with potential applications to multijunction solar cells and VCSELs [11], and III-nitride nanostructured TJs taking advantage of the strong polarization fields at heterointerfaces have been proposed to improve the efficiency of UV light-emitting diodes (LEDs) [12]. In these cases, the spectral selectivity of the nanostructure adds to the complexity of the tunneling process [13].

The challenge of developing an accurate, yet computationally feasible, model of TJ-VCSELs is to combine a rigorous description of quantum transport in the tunneling region, including the relevant density of states and associated current flow under nonequilibrium conditions, with a semiclassical drift-diffusion (DD) picture in the adjacent bulk layers, where quasiequilibrium statistics may be assumed. The multiscale nature of the problem is usually addressed by correcting intrinsically local semiclassical approaches with generation-recombination (GR) rates accounting for the interband tunneling process. However, conventional quantum-corrected drift-diffusion codes [14–21] struggle with the large number of simplifying assumptions on the density of states participating in the tunneling, the occupation of these states, carrier confinement, and the nature of the scattering mechanisms assisting the tunneling.

Following the seminal work of Kane [22], different local-recombination tunneling models have been proposed

*alberto.tibaldi@polito.it

[23,24] but their applicability is usually limited to specific operating conditions [25,26]. For example, it is known that Hurkx's model may significantly underestimate the tunneling current due to the saturation of the net generation rate, unless the recombination rate is neglected—which, however, violates the detailed balance principle at equilibrium [27]. On the other hand, nonlocal models [28–30] achieve flexibility by allowing carriers to be generated at different locations, i.e., introducing real space transport across the junction, but their success in reproducing experimental data seems to be based much less on the correct description of the underlying physics than the high number of adjustable parameters involved.

Section II describes the quantum-corrected DD solver; the corrections are obtained from a nonequilibrium Green's function (NEGF) approach applied to the regions of the VCSEL where quantum effects are relevant. In Sec. III, the simulator is validated with the electrical measurements of a TJ-VCSEL test structure designed and characterized at Chalmers University. Inspection of the relevant microscopic quantities provides insights into the mechanisms assisting the tunneling process. The interpretation of the experimental results provides guidelines for future prototypes.

II. THEORY

In contrast to non-self-consistent quantum models of tunneling, where tunneling probabilities are evaluated from the Schrödinger's equation with frozen potential profiles and closed boundary conditions [29], here we propose a self-consistent solution of NEGF and DD equations, as required for the analysis of TJ-VCSELs.

Multiscale NEGF-DD models are usually implemented by partitioning the simulation domain in a nonequilibrium region treated within the NEGF approach and quasiequilibrium regions described within the DD approximation. Current continuity is enforced at NEGF/DD interfaces, with the nonequilibrium region considered as the current-limiting element of the device [31–34]. As an alternative to this partitioning approach, we propose a DD simulation of the whole VCSEL structure, quantum-corrected with a NEGF-derived GR rate to describe the tunneling current. We believe that this approach is more appropriate for TJ-based optoelectronic devices, because it naturally allows for both space and energy separation of the quantum (NEGF) and bulk (DD) regions. The NEGF current can be restricted to just the interband tunneling component by integrating the spectral current density in an appropriate energy range, while the *classical* intraband component (essentially the leakage current) is still captured by the DD approach. The same concept could also be applied to the active region of the VCSEL (not included in the prototype structure under consideration), in which the interband current is due to radiative recombination.

A schematic overview of the self-consistent NEGF-DD algorithm is shown in Fig. 1. The steady-state Keldysh and the Dyson equations are iteratively solved in the NEGF space-energy window with the Hartree potential obtained from the DD band diagram. A finite-element discretization leads to a coupled set of equations that are parametrically dependent on the transverse wave vector $\mathbf{k}$ and the energy E [35–37]

$$\left[EM - H(\mathbf{k}) - \Sigma^R(\mathbf{k},E)\right] G^R(\mathbf{k},E) = I, \tag{1a}$$

$$G^{\lessgtr}(\mathbf{k},E) = G^R(\mathbf{k},E)\Sigma^{\lessgtr}(\mathbf{k},E)G^A(\mathbf{k},E). \tag{1b}$$

Due to the nonorthogonality of the finite-element basis functions, contravariant- and covariant-matrix representations are used for the Green's functions and self-energies, respectively, the two representations being related by the overlap matrix M. Since tunneling is sensitive to the details of the evanescent bands within the band gap of the material, we describe the electronic structure with a multiband 8×8 $\mathbf{k}\cdot\mathbf{p}$ model including the first conduction band and heavy-hole, light-hole, and split-off bands [38,39]. In principle, $\mathbf{k}\cdot\mathbf{p}$ parameters should be derived from full-Brillouin-zone band-structure calculations [40], but we adopt the semiempirical Luttinger parameters reported in Ref. [41]. The nanostructure Hamiltonian $H(\mathbf{k})$ and the boundary self-energies $\Sigma_B^{R\lessgtr}$ reflecting the openness of the system are reported in the Appendix.

Coupling to acoustic and polar optical phonons is considered within the deformation potential and the Fröhlich formalism, respectively, by means of fully nonlocal electron-phonon (ep) self-energies $\Sigma_{\text{ep}}^{R\lessgtr}$ computed in the

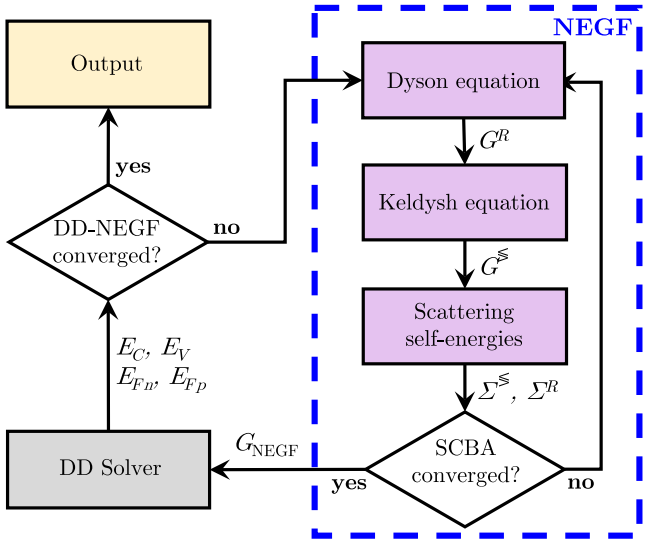

FIG. 1. The work flow of the simulation framework, featuring an inner NEGF loop marked with the blue dashed box, coupled self-consistently with a DD solver.

self-consistent Born approximation [35]

$$\left[\Sigma_{\rm ep}^{\lessgtr}(\mathbf{k},E)\right]_{\alpha\beta} = \sum_{\mathbf{Q}} |U_Q|^2 e^{iq_z(z_i-z_j)} \left[M\left(N_Q G^{\lessgtr}(\mathbf{k}-\mathbf{q},E\mp\hbar\omega_{\mathbf{Q}}) + (N_Q+1)G^{\lessgtr}(\mathbf{k}-\mathbf{q},E\pm\hbar\omega_{\mathbf{Q}})\right)M\right]_{\alpha\beta}, \quad (2)$$

where $\alpha = (a,i)$ and $\beta = (b,j)$ are compound indices representing bands a and b and mesh nodes i and j. The occupation numbers N_Q of (three-dimensional, 3D) phonons with wave vectors $\mathbf{Q} = (\mathbf{q}, q_z)$ are computed according to Bose-Einstein statistics. Neglecting the principal-part integral, which just leads to energy renormalization, the retarded component of the self-energy reads [42]

$$\begin{aligned}\left[\Sigma_{\rm ep}^{R}(\mathbf{k},E)\right]_{\alpha\beta} &= \sum_{\mathbf{Q}} |U_Q|^2 e^{iq_z(z_i-z_j)} \Big[M\Big(N_Q\, G^R(\mathbf{k}-\mathbf{q},E+\hbar\omega_{\mathbf{Q}}) \\ &+ (N_Q+1)\, G^R(\mathbf{k}-\mathbf{q},E-\hbar\omega_{\mathbf{Q}}) \\ &+ \frac{1}{2}G^<(\mathbf{k}-\mathbf{q},E-\hbar\omega_{\mathbf{Q}}) \\ &- \frac{1}{2}G^<(\mathbf{k}-\mathbf{q},E+\hbar\omega_{\mathbf{Q}})\Big)M\Big]_{\alpha\beta}. \end{aligned} \quad (3)$$

According to deformation-potential theory, the scattering strength U_Q due to the interaction with acoustic modes is described by

$$U_Q = \sqrt{\frac{\hbar D_a^2}{2V\rho u_l}Q}, \quad (4)$$

where u_l is the longitudinal sound velocity in the material, D_a is the deformation potential coupling constant [[43], Ch. 5], ρ is the semiconductor mass density, and V is the normalization volume. The material parameters are listed in Table I.

Assuming a dispersionless longitudinal optical phonon with energy $\hbar\omega_{\rm LO}$, the Fröhlich theory of polar optical scattering gives

$$U_Q = \sqrt{\frac{e^2\hbar\omega_{\rm LO}}{2V}\left(\frac{1}{\epsilon_\infty}-\frac{1}{\epsilon_s}\right)}\frac{Q}{Q^2+q_0^2}, \quad (5)$$

where ϵ_s and ϵ_∞ are the static and optical dielectric constants of the material, e is the elementary charge, and q_0 is the inverse of the Debye-Hückel screening length (10 nm in all the simulations below).

Upon convergence of the self-consistent Born cycle, the divergence of the current density [the trace is over zone-center basis functions, $\Delta_i \equiv 0.5(z_{i+1}-z_{i-1})$ and A is the normalization area]

$$\frac{\partial J_{\rm NEGF}}{\partial z}(z_i) = \frac{e}{\hbar A\Delta_i}\sum_{\mathbf{k}}\int\frac{dE}{2\pi}\,{\rm Tr}[H(\mathbf{k})G^<(\mathbf{k},E) - G^<(\mathbf{k},E)H(\mathbf{k})]_{ii} \quad (6)$$

should vanish upon energy integration over the whole energy range, including both conduction and valence bands. If the integration is restricted to one of the two bands, the right-hand side of Eq. (6) provides the local GR rate to be included in the DD continuity equations

$$G_{\rm NEGF}(z) = \frac{1}{e}\frac{dJ_{n,\rm NEGF}}{dz} = -\frac{1}{e}\frac{dJ_{p,\rm NEGF}}{dz}. \quad (7)$$

The band-to-band tunneling (BTBT) generation rate (7) is added to the other GR mechanisms present in the DD simulation, e.g., the Shockley-Read-Hall (SRH), radiative, and Auger rates [36].

As conduction- and valence-band states coexist in the same energy region (the tunneling window), a local midgap energy threshold is used to separate the electron and hole contributions to the spectral current. Considering the possible presence of field-induced subgap states, this choice may appear somewhat arbitrary. However, as long as the electron and hole populations are well defined at the borders of the NEGF simulation domain, which is a necessary condition for a bipolar DD approach to make sense, the choice of this local threshold only changes the spatial profile of $G_{\rm NEGF}(z)$, but not its integral, i.e., the tunneling current.

The quasi-Fermi levels associated with the majority carriers are pinned on both sides of the TJ, providing well-defined Fermi levels for the calculation of the boundary self-energies. The NEGF region should obviously include the tunneling junction but also a portion of the surrounding layers to account for the possible quantization effects caused by the unintentional heterostructures created by the band-gap-narrowing induced by the sharp doping profiles needed to achieve a low tunneling resistance.

TABLE I. The material parameters used in the NEGF simulations.

Quantity	Value	Description
D_a	8	Deformation potential (eV)
ρ	5.3	Mass density (g/cm^3)
u_l	5240	Sound velocity (m/s)
$\hbar\omega_{\rm LO}$	36	LO phonon energy (meV)
ε_s	$12.9\varepsilon_0$	Static permittivity (F/m)
ε_∞	$10.9\varepsilon_0$	Optical permittivity (F/m)

III. RESULTS

The TJ test structure (n-n^+p^+-p-i-n) under consideration is sketched in Fig. 2. The n^+p^+ tunneling junction is similar to the one investigated in Ref. [11], but operated in reverse bias to allow for VCSEL operation. The selectively oxidized $Al_{0.98}Ga_{0.02}As$ layer below the TJ is needed to obtain current confinement and to minimize surface recombination. No quantum wells are included within the p-i-n junction of this prototype structure, since the focus of this investigation is on the electrical properties. Except for the TJ, where tellurium is used to enable high n-doping levels [44,45], all other layers are n-type doped with silicon and p-type doped with carbon.

Quasi-3D DD simulations [21] suggest that the current flow is almost vertical and uniform within the oxide aperture, since the device is very short in the transport direction z. The negligible lateral current spreading justifies the one-dimensional approach adopted here [46]. An effective oxide aperture of 18 μm is estimated and a 6 Ω series resistance is included to account for nonideal contacts and substrate.

Figure 3 shows the simulated band diagram of the device at 2.2 V. Part of the bias voltage drops across the series resistance, resulting in an overall 1.75-eV quasi-Fermi-level splitting at the boundary of the DD simulation domain, driving the TJ in reverse bias and the pin heterostructure in forward bias. The barrier in the valence band due to the aluminum-rich layer needed for wet oxidation is clearly visible (layer 4 in the TJ-VCSEL stack). The inset shows an enlargement of the band diagram in the region where the NEGF analysis is performed (green box), which includes the TJ and part of the p buffer (layers

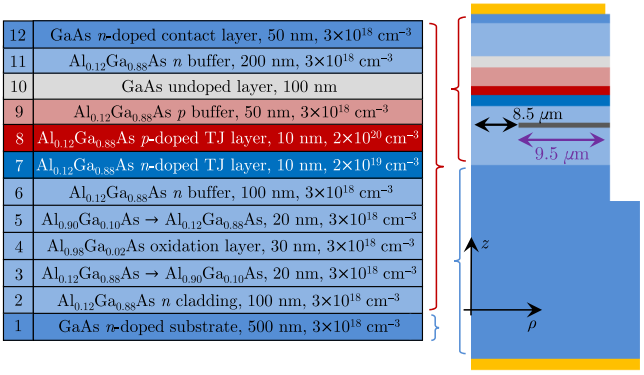

FIG. 2. A sketch of the device under analysis, including layer details. The geometry has cylindrical symmetry. The ground contact is placed below the substrate. The $Al_xGa_{1-x}As$ structure is grown on top of it. The 17-μm oxide aperture is obtained from wet oxidation of the layer with high Al content. The dark-blue and dark-red layers form the TJ. The light-gray layer indicates the undoped region. The structure ends with a top contact layer, with an ohmic metal contact on top. The red and blue regions indicate p- and n-type materials, respectively.

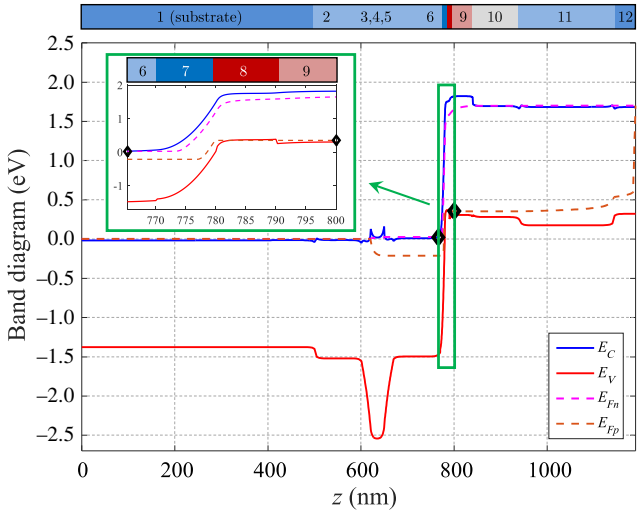

FIG. 3. A simulated band diagram of the device under analysis at 2.2 V bias. The conduction- and valence-band edges and the electron and hole quasi-Fermi levels are represented by solid blue, solid red, dashed magenta, and dashed brown lines, respectively. The band diagram of the TJ is enlarged in the inset. The black diamonds represent the quasi-Fermi levels of the majority carriers at the boundaries of the NEGF simulation window.

7–9). Band-gap-narrowing effects caused by doping density discontinuities in the TJ [47] create an unintentional double heterostructure between layers 7 and 9. The electron and hole quasi-Fermi levels are pinned very close to the corresponding band edges at the borders of the TJ. Even though tellurium has a higher ionization energy than silicon [48], the donors are fully ionized, while the acceptors are only partially ionized in the asymmetrically doped TJ.

The stripelike pattern of the spectral current density in Fig. 4 (bottom) is indicative of resonant tunneling across the TJ. The resonances are related to the presence of confined states in the QW induced by band-gap narrowing in the valence band of layer 8 [see the local density of states (LDOS) in Fig. 4 (top)]. Additional confined states corresponding to the split-off band do not participate in the tunneling process [see the LDOS peaks at the lower border of the tunneling window (the red stripes near 0 eV)]. The corresponding energy-integrated spatial-dependent GR rate G_{NEGF} (dashed line) is peaked where the tunneling path is shortest.

Phonon-assisted tunneling is usually discussed in the context of indirect-band-gap semiconductors [49–51], where the band-gap states connecting the valence and conduction bands are not purely imaginary, and tunneling requires the absorption or emission of a phonon to ensure conservation of momentum [52]. In direct band-gap semiconductors, symmetry arguments suggest that electron-phonon coupling is inefficient across the TJ [53]. Carrier-phonon scattering may even slightly decrease the

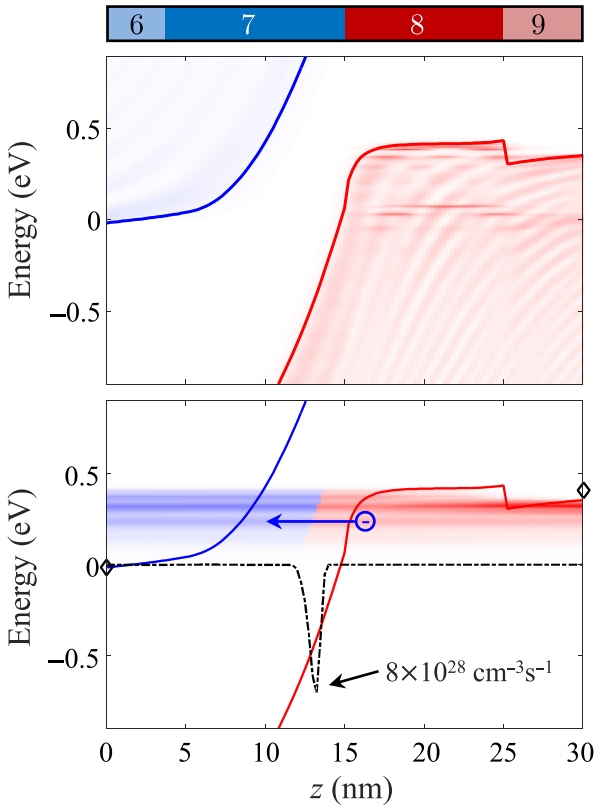

FIG. 4. Top: the local density of states computed for a zero transverse wave vector, resolved in position and energy. Bottom: the current density resolved in position and energy; the blue and red shading indicates the electron and hole contributions, respectively. The dashed-dotted black curve represents the spatial profile of G_{BTBT} (the peak value is 8×10^{28} cm^{-3} s^{-1}).

tunneling current with respect to the coherent case, as observed in InAs tunnel field-effect transistors, an effect attributed to the backscattering of electrons on their way from the source to the drain [52]. In general, the role of phonon-assisted tunneling in direct material systems is to open additional transmission paths, not accessible by coherent transport, when a direct BTBT window does not exist [13]. This does not mean that the interaction with phonons does not contribute to the determination of the BTBT current. In the specific case considered here, the two processes (coherent interband tunneling and phonon interaction) are sequential rather than simultaneous, and so, strictly speaking, the tunneling process is mainly a coherent process (i.e., phononless), as expected for systems with a direct band gap, but it would be underestimated without inelastic polar optical scattering, which is needed to reveal and populate the confined states in layer 8, otherwise unreachable from the contacts. Similar behavior is observed in multijunction solar cells, in which, depending on the bias conditions, the states feeding the tunneling current may not be accessible without energy relaxation and, likewise, the electrons tunnelling to the doping-induced QW, on the other side of the junction, may not be able to escape to the contact, unless electron-phonon scattering is present [1].

Trap-assisted tunneling (TAT) is not included in the simulation, as the presence of defects is not expected to reduce the relatively short tunneling path induced by the large band bending under strong reverse bias. On the other hand, TAT may play an important role if the TJ is operated in forward bias, when the energy window for direct tunneling disappears [54]. It is generally understood that the excess current (also known as the valley current, i.e., the additional current beyond the tunneling peak that cannot be classified as a diffusion current; see Fig. 1 of Ref. [55]) is dominated by tunneling through midgap states. TAT may be enhanced by inelastic phonon scattering, with defect states acting as stepping stones for the tunneling process [56]. Perhaps the most convincing experimental evidence of TAT is the high ideality factor observed below the optical turn-on of GaN-based light-emitting diodes (LEDs), which has been attributed to TAT mediated by SRH recombination centers located in the LED active region [57]. The treatment of TAT within a NEGF formalism requires the inclusion of additional Dyson and Keldysh equations for the trap levels [58]. As TAT is relevant only for TJs in the weak forward-bias regime, we postpone this analysis to a future work.

Figure 5 shows the *I*-*V* (blue) and *R*-*I* (red) characteristics of the TJ-VCSEL under study. Satisfactory agreement is obtained between simulation (solid curves) and measurement (circles). The TJ doping concentrations, known to within a factor of 2–5, are used as the only fitting parameters. Self-consistency is achieved after 5–7 DD/NEGF iterations for each bias point.

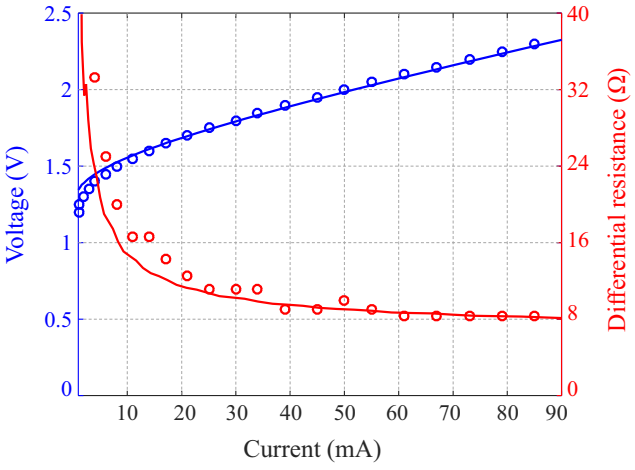

FIG. 5. The *I*-*V* (blue curves, left-hand scale) and *R*-*I* (red curves, right-hand scale) characteristics of the device under study. The simulation and experimental results are represented using solid curves and open bullets, respectively.

The I-V characteristics alone may be misleading in the assessment of the TJ performance. Inspection of the spatial dependence of the electron and hole currents (see Fig. 6, left) reveals that the tunneling current is small compared to the total current. The tunneling process generates opposite but equal charges on both sides of the junction, the strongly localized carrier generation resulting in the seeming discontinuities in the electron and hole currents. The unbalance of these two components across the junction, which cannot be identified by simple I-V measurements, is therefore indicative of an additional contribution.

The electron and hole currents evaluated on the p side of the TJ (layer 8) from the fully scattered Green's functions are shown versus the applied bias in the right panel of Fig. 6 (red and blue solid lines, respectively). The coherent results (dashed-dotted lines) slightly underestimate the current due to the impossibility of reaching the confined states supported by the doping-induced heterostructure. On this side of the junction, the hole current is the tunneling current, while the electron current can be interpreted as a leakage current (not contributing to radiative recombination), which sets in when the accumulation of holes lowers the barrier associated with the other p-n junction of the structure, the one that should include the active region, on the right-hand side of Fig. 3.

It helps to conceive the structure under study as a phototransistor consisting of two junctions connected back to back, the already discussed reverse-biased TJ and the forward-biased VCSEL junction. The tunneling current plays the role of the photocurrent, enabling an electron flow from the emitter (layers 11–12) to the collector (layers 1–7). The current gain results from normal transistor action, if the lifetime of the injected electrons in the base is longer than the transit time across the base (layers 8–10). The large leakage current is just the result of the negligible radiative recombination in the intrinsic region (the prototype structure under consideration does not include any QWs). The introduction of five QWs in the intrinsic layer 10, where the electrons from the "emitter" can recombine by spontaneous emission with the holes injected by the TJ, almost suppresses the leakage current, as shown in Fig. 7. The absence of the active region in the experimentally investigated structure does not prevent the observation of a tunneling current, nor the assessment of the TJ performance, since the leakage current is proportional to the tunneling current (without tunneling, the TJ junction would support only a very small inverse saturation current, preventing the VCSEL diode from conducting). It is interesting to note that even in the presence of five QWs, the leakage current is small but not exactly zero. The role of carrier leakage is almost unexplored in TJ-VCSELs; however, leaking electrons may potentially be swept by the strong electric fields in the reverse-biased TJ. Electron blocking layers (EBLs) are commonly employed in GaN-based VCSELs and LEDs, in which carrier confinement is reduced by the strong polarization fields [59]. The performance of a regular 850-nm $In_xAl_yGa_{1-x-y}As/Al_xGa_{1-x}As$ VCSEL could be enhanced if an EBL is employed [60].

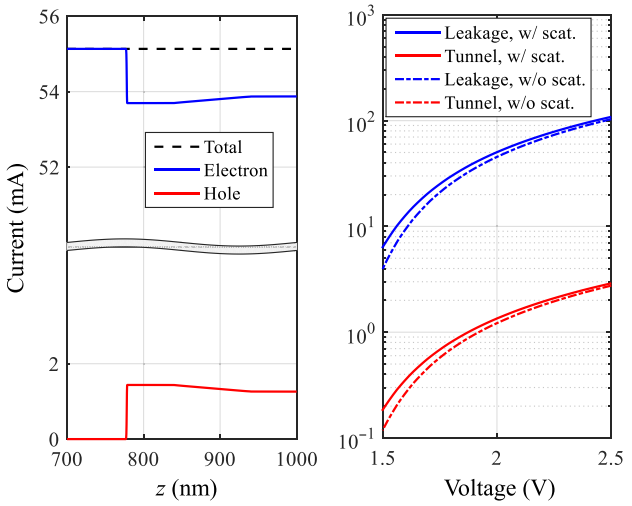

FIG. 6. The currents in the device under test. Left: spatial profiles of the electron, hole, and total currents at a bias of 2.2 V (the voltage drop across the series resistance is 0.5 V), shown using solid blue, solid red, and dashed black lines, respectively. Right: the I-V characteristics evaluated on the p side of the TJ ($z = 783$ nm). The electron (leakage) and hole (tunneling) currents computed from fully scattered Green's functions are shown as solid blue and red lines, respectively. The corresponding currents in the coherent limit are represented by dashed-dotted lines.

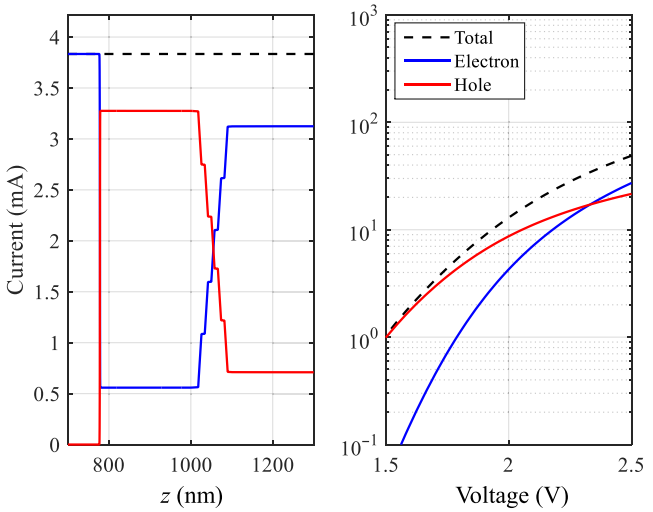

FIG. 7. The currents in the device under test, modified to include five $In_{0.2}Ga_{0.8}As$ QWs in the GaAs undoped region 10. Left: the spatial profiles of the electron, hole, and total currents at a bias of 1.72 V (the voltage drop across the series resistance is negligible), shown using solid blue, solid red, and dashed black lines, respectively. Right: the I-V characteristics evaluated on the p side of the TJ ($z = 783$ nm).

The present NEGF-DD approach provides a rigorous formalism to describe carrier leakage, since it combines the DD capability of modeling realistic macroscopic structures with the energy-resolved description of optical transitions and transport processes on an equal footing, afforded by NEGF. We will postpone a complete analysis of TJ-VCSELs, including the lasing modes of the VCSEL cavity, to a future work.

IV. CONCLUSION

This paper describes a multiscale strategy for the simulation of (opto)electronic devices based on a quantum-corrected semiclassical approach, with NEGF-derived GR rates bridging the gap between drift diffusion and quantum transport. The identification of the different current components (tunneling versus leakage) is just another example on the importance of rigorous quantum transport modeling for the correct interpretation of experimental investigations concerning loss mechanisms in light emitters [59,61]. Future works will deal with the multiphysics simulation of TJ-VCSELs by including the present approach in our Vcsel Electro-opto-thermal NUmerical Simulator VENUS [21].

ACKNOWLEDGMENTS

This work was supported in part by the U.S. Army Research Laboratory through the Collaborative Research Alliance (CRA) for MultiScale multidisciplinary Modeling of Electronic materials (MSME). The computational resources were provided by HPC@POLITO, the U.S. Department of Defense (DoD) High-Performance Computing (HPC) Systems, and the 2019 Army Research Office Defense University Research Instrumentation Program (DURIP) Award (Grant No. W911NF-19-1-0161) made to Dr. E. Bellotti.

APPENDIX: HAMILTONIAN AND BOUNDARY SELF-ENERGIES

The starting point of the finite-element discretization of the Dyson and Keldysh equations is the eight-band Pidgeon-Brown or Enders $\mathbf{k}\cdot\mathbf{p}$ Hamiltonian [62]

$$H_{\mathbf{k}\cdot\mathbf{p}} = \begin{bmatrix} E_g + A_c(k_x^2+k_y^2+k_z^2) & iPk_x & iPk_y & iPk_z \\ -iPk_x & Lk_x^2 + M(k_y^2+k_z^2) - \Delta/3 & Nk_xk_y - i\Delta/3 & k_xN_+k_z + k_zN_-k_x \\ -iPk_y & Nk_xk_y + i\Delta/3 & Lk_y^2 + M(k_x^2+k_z^2) - \Delta/3 & k_yN_+k_z + k_zN_-k_y \\ -iPk_z & k_zN_+k_x + k_xN_-k_z & k_zN_+k_y + k_yN_-k_z & Lk_z^2 + M(k_x^2+k_y^2) - \Delta/3 \\ 0 & 0 & 0 & 0 \\ 0 & 0 & 0 & -\Delta/3 \\ 0 & 0 & 0 & -i\Delta/3 \\ 0 & \Delta/3 & i\Delta/3 & 0 \end{bmatrix}$$

$$\begin{bmatrix} 0 & 0 & 0 & 0 \\ 0 & 0 & 0 & \Delta/3 \\ 0 & 0 & 0 & -i\Delta/3 \\ 0 & -\Delta/3 & i\Delta/3 & 0 \\ E_g + A_c(k_x^2+k_y^2+k_z^2) & iPk_x & iPk_y & iPk_z \\ -iPk_x & Lk_x^2 + M(k_y^2+k_z^2) - \Delta/3 & Nk_xk_y + i\Delta/3 & k_xN_+k_z + k_zN_-k_x \\ -iPk_y & Nk_xk_y - i\Delta/3 & Lk_y^2 + M(k_x^2+k_z^2) - \Delta/3 & k_yN_+k_z + k_zN_-k_y \\ -iPk_z & k_zN_+k_x + k_xN_-k_z & k_zN_+k_y + k_yN_-k_z & Lk_z^2 + M(k_x^2+k_y^2) - \Delta/3 \end{bmatrix}, \tag{A1}$$

in the zone-center basis

$$S\uparrow, X\uparrow, Y\uparrow, Z\uparrow, S\downarrow, X\downarrow, Y\downarrow, Z\downarrow, \tag{A2}$$

where E_g is the fundamental gap of the unstrained material, Δ is the spin-orbit splitting, P is the interband momentum matrix element, the renormalized parameters A_c, L, M, and N are obtained from the conduction-band effective mass m_c^*, and the modified Luttinger parameters [37,63]. According to operator ordering, the Kane parameter N is split into two asymmetric parts $N = N_+ + N_-$, with $N_- = M - \hbar^2/(2m_0)$. The splitting is shown only for the matrix elements of Eq. (A1) that are linear in k_z, assuming that z is the only symmetry-broken direction.

Moving to the atomiclike basis set defined in Ref. [38,39] and adopting the axial approximation, the bulk

Hamiltonian block-diagonalizes with respect to the spin components (i.e., the 8×8 Hamiltonian decouples into two 4×4 blocks) and the energy dispersion becomes isotropic in the transverse wave vector. Rewriting the bulk $\mathbf{k} \cdot \mathbf{p}$ Hamiltonian as

$$H_{\mathbf{k}\cdot\mathbf{p}}(\mathbf{k}, k_z) = H_2(\mathbf{k})k_z^2 + H_1(\mathbf{k})k_z + H_0(\mathbf{k}) \tag{A3}$$

and replacing the wave vector k_z of the quantized direction z with the corresponding operator $-i\partial_z$ gives the differential operator,

$$H(\mathbf{k}) = -\partial_z H_2 \partial_z + H_{1L}\partial_z + \partial_z H_{1R} + H_0, \tag{A4}$$

to which the finite-element procedure is applied to obtain the nanostructure Hamiltonian. Open boundary conditions are obtained by solving the complex band-structure problem [64,65], which means fixing $\mathbf{k} = (k_x, k_y)$ and looking for k_z-value solutions of the quadratic (generalized) eigenvalue problem associated with Eq. (A3). Selecting the Bloch waves propagating or decaying away from the contact, we find the corner blocks of the boundary self-energy:

$$\Sigma_{\pm}^{RB}(\mathbf{k}, E) = \mp H_2 U_{\pm} \Lambda_{\pm} U_{\pm}^{-1} \mp i H_{1R}, \tag{A5}$$

where $\Lambda_{\pm}$ is a diagonal matrix the diagonal elements of which are the $k_z^{\pm}$ solutions propagating (real k_z values with group velocity $v_g(k_z) \gtrless 0$) or decaying (complex k_z values with $\mathrm{Im}(k_z) \gtrless 0$) away from the right (upper signs) and the left (lower signs) contacts and the columns of $U_{\pm}$ are the corresponding eigenvectors. The lesser and greater components of the boundary self-energy are computed from the fluctuation-dissipation theorem.

[1] U. Aeberhard, Theoretical investigation of direct and phonon-assisted tunneling currents in InAlGaAs/InGaAs bulk and quantum-well interband tunnel junctions for multijunction solar cells, Phys. Rev. B **87**, 081302(R) (2013).

[2] P. Colter, B. Hagar, and S. Bedair, Tunnel junctions for III-V multijunction solar cells review, Crystals **8**, 445 (2018).

[3] G. Gupta, B. Rajasekharan, and R. J. E. Hueting, Electrostatic doping in semiconductor devices, IEEE Trans. Electron Devices **64**, 3044 (2017).

[4] V. Fan Arcara, B. Damilano, G. Feuillet, S. Vézian, K. Ayadi, S. Chenot, and J.-Y. Duboz, Ge doped GaN and $Al_{0.5}Ga_{0.5}N$-based tunnel junctions on top of visible and UV light emitting diodes, J. Appl. Phys. **126**, 224503 (2019).

[5] S. Lee, C. A. Forman, J. Kearns, J. T. Leonard, D. A. Cohen, S. Nakamura, and S. P. DenBaars, Demonstration of GaN-based vertical-cavity surface-emitting lasers with buried tunnel junction contacts, Opt. Express **27**, 31621 (2019).

[6] W. Hofmann, High-speed buried tunnel junction vertical-cavity surface-emitting lasers, IEEE Photon. J. **2**, 802 (2010).

[7] S. Spiga, W. Soenen, A. Andrejew, D. M. Schoke, X. Yin, J. Bauwelinck, G. Boehm, and M.-C. Amann, Single-mode high-speed 1.5 μm VCSELs, J. Lightwave Technol. **35**, 727 (2017).

[8] V. Jayaraman, M. Mehta, A. W. Jackson, S. Wu, Y. Okuno, J. Piprek, and J. E. Bowers, High-power 1320-nm wafer-bonded VCSELs with tunnel junctions, IEEE Photon. Technol. Lett. **15**, 1495 (2003).

[9] V. Iakovlev, G. Suruceanu, A. Caliman, A. Mereuta, A. Mircea, C.-A. Berseth, A. Syrbu, A. Rudra, and E. Kapon, High-performance single-mode VCSELs in the 1310-nm waveband, IEEE Photon. Technol. Lett. **17**, 947 (2005).

[10] A. Caliman, A. Mereuta, P. Wolf, A. Sirbu, V. Iakovlev, D. Bimberg, and E. Kapon, 25 Gbps direct modulation and 10 km data transmission with 1310 nm waveband wafer fused VCSELs, Opt. Express **24**, 16329 (2016).

[11] K. Louarn, Y. Claveau, L. Marigo-Lombart, C. Fontaine, A. Arnoult, F. Piquemal, A. Bounouh, N. Cavassilas, and G. Almuneau, Effect of low and staggered gap quantum wells inserted in GaAs tunnel junctions, J. Phys. D **51**, 145107 (2018).

[12] Y. Zhang, Z. Jamal-Eddine, and S. Rajan, Recent progress of tunnel junction-based ultra-violet light emitting diodes, Japan. J. Appl. Phys. **58**, SC0805 (2019).

[13] U. Aeberhard, The nonequilibrium Green's function picture of inelastic processes in nanostructure photovoltaics, J. Comp. Electron. **15**, 1219 (2016).

[14] N. Tessler, and G. Eisenstein, On carrier injection and gain dynamics in quantum well lasers, IEEE J. Quantum Electron. **QE-29**, 1586 (1993).

[15] G. A. Baraff, Model for the effect of finite phase-coherence length on resonant transmission and capture by quantum wells, Phys. Rev. B **58**, 13799 (1998).

[16] M. Grupen, and K. Hess, Simulation of carrier transport and nonlinearities in quantum-well laser diodes, IEEE J. Quantum Electron. **34**, 120 (1998).

[17] B. Witzigmann, A. Witzig, and W. Fichtner, A multidimensional laser simulator for edge-emitters including quantum carrier capture, IEEE Trans. Electron Devices **47**, 1926 (2000).

[18] C. De Santi, M. Meneghini, A. Tibaldi, M. Vallone, M. Goano, F. Bertazzi, G. Verzellesi, G. Meneghesso, and E. Zanoni, in Nitride Semiconductor Light-Emitting Diodes, edited by J. J. Huang, H. C. Kuo, and S.-C. Shen (Woodhead Publishing, Duxford, UK, 2018), 2nd ed., Chap. 14, p. 455.

[19] K. Mehta, Y.-S. Liu, J. Wang, H. Jeong, T. Detchprohm, Y. J. Park, S. R. Alugubelli, S. Wang, F. A. Ponce, S.-C. Shen, R. D. Dupuis, and P. D. Yoder, Lateral current spreading in III-N ultraviolet vertical-cavity surface-emitting lasers using modulation-doped short period superlattices, IEEE J. Quantum Electron. **54**, 2400507 (2018).

[20] A. P. Cédola, D. Kim, A. Tibaldi, M. Tang, A. Khalili, J. Wu, H. Liu, and F. Cappelluti, Physics-based modeling and experimental study of Si-doped InAs/GaAs quantum dot solar cells, Int. J. Photoenergy **2018**, 7215843 (2018).

[21] A. Tibaldi, F. Bertazzi, M. Goano, R. Michalzik, and P. Debernardi, VENUS: A Vertical-cavity surface-emitting laser Electro-opto-thermal NUmerical Simulator, IEEE J. Select. Topics Quantum Electron. **25**, 1500212 (2019).

[22] E. O. Kane, Theory of tunneling, J. Appl. Phys. **32**, 83 (1961).

[23] G. A. M. Hurkx, D. B. M. Klaassen, and M. P. G. Knuvers, A new recombination model for device simulation including tunneling, IEEE Trans. Electron Devices **39**, 331 (1992).

[24] A. Schenk, Rigorous theory and simplified model of the band-to-band tunneling in silicon, Solid-State Electron. **36**, 19 (1993).

[25] M. Vallone, M. Mandurrino, M. Goano, F. Bertazzi, G. Ghione, W. Schirmacher, S. Hanna, and H. Figgemeier, Numerical modeling of SRH and tunneling mechanisms in high-operating-temperature MWIR HgCdTe photodetectors, J. Electron. Mater. **44**, 3056 (2015).

[26] N. Moulin, M. Amara, F. Mandorlo, and M. Lemiti, Tunnel junction $I(V)$ characteristics: Review and a new model for p-n homojunctions, J. Appl. Phys. **126**, 033105 (2019).

[27] H.-Y. Wong, D. Dolgos, L. Smith, and R. V. Mickevicius, Modified Hurkx band-to-band-tunneling model for accurate and robust TCAD simulations, Microelectron. Reliability **104**, 113552 (2020).

[28] M. Ieong, P. M. Solomon, S. Laux, H.-S. P. Wong, and D. Chidambarrao, in 1998 IEEE International Electron Devices Meeting (IEDM '98) (San Francisco, CA, USA, 1998), p. 733.

[29] D. Esseni, M. Pala, P. Palestri, C. Alper, and T. Rollo, A review of selected topics in physics based modeling for tunnel field-effect transistors, Semiconductor Sci. Technol. **32**, 083005 (2017).

[30] A. Schenk, and S. Sant, Tunneling between density-of-state tails: Theory and effect on Esaki diodes, J. Appl. Phys. **128**, 014502 (2020).

[31] G. Klimeck, Quantum and semi-classical transport in NEMO 1-D, J. Comp. Electron. **2**, 177 (2003).

[32] M. Auf Der Maur, Multiscale approaches for the simulation of optoelectronic devices, J. Green Eng. **5**, 133 (2015).

[33] J. Geng, P. Sarangapani, E. Nelson, C. Wordelman, B. Browne, T. Kubis, and G. Klimeck, in *16th International Conference on Numerical Simulation of Optoelectronic Devices (NUSOD 2016)* (IEEE, Sydney, Australia, 2016), p. 107.

[34] T. A. Ameen, H. Ilatikhameneh, J. Z. Huang, M. Povolotskyi, R. Rahman, and G. Klimeck, Combination of equilibrium and nonequilibrium carrier statistics into an atomistic quantum transport model for tunneling heterojunctions, IEEE Trans. Electron Devices **64**, 2512 (2017).

[35] S. Steiger, Ph.D. thesis, Eidgenössische Technische Hochschule Zürich, 2009.

[36] F. Bertazzi, M. Goano, G. Ghione, A. Tibaldi, P. Debernardi, and E. Bellotti, in *Handbook of Optoelectronic Device Modeling and Simulation*, edited by J. Piprek (CRC Press, Boca Raton, FL, 2017), Chap. 2, p. 35.

[37] F. Bertazzi, A. Tibaldi, M. Goano, J. A. Gonzalez Montoya, and E. Bellotti, Non-equilibrium Green's function modeling of type-II superlattice detectors and its connection to semiclassical approaches, Phys. Rev. Appl. **14**, 014083 (2020).

[38] P.-F. Qiao, S. Mou, and S. L. Chuang, Electronic band structures and optical properties of type-II superlattice photodetectors with interfacial effect, Opt. Express **20**, 2319 (2012).

[39] G. Liu, and S.-L. Chuang, Modeling of Sb-based type-II quantum cascade lasers, Phys. Rev. B **65**, 165220 (2002).

[40] X. Zhou, F. Bertazzi, M. Goano, G. Ghione, and E. Bellotti, Deriving $k \cdot p$ parameters from full-Brillouin-zone descriptions: A finite-element envelope function model for quantum-confined wurtzite nanostructures, J. Appl. Phys. **116**, 033709 (2014).

[41] I. Vurgaftman, J. R. Meyer, and L. R. Ram-Mohan, Band parameters for III-V compound semiconductors and their alloys, J. Appl. Phys. **89**, 5815 (2001).

[42] U. Aeberhard, and R. H. Morf, Microscopic nonequilibrium theory of quantum well solar cells, Phys. Rev. B **77**, 125343 (2008).

[43] K. Hess, ed., *Monte Carlo Device Simulation: Full Band and Beyond* (Kluwer Academic Publishers, Boston, 1991).

[44] H. K. Kang, S.-H. Park, D. H. Jun, C. Z. Kim, K. M. Song, W. Park, C. G. Ko, and H. Kim, Te doping in the GaAs tunnel junction for GaInP/GaAs tandem solar cells, Semiconductor Sci. Technol. **26**, 075009 (2011).

[45] X. Gan, X. Zheng, Y. Wu, S. Lu, H. Yang, M. Arimochi, T. Watanabe, M. Ikeda, I. Nomachi, and H. Yoshida, GaAs tunnel junction grown using tellurium and magnesium as dopants by solid-state molecular beam epitaxy, Japan. J. Appl. Phys. **53**, 021201 (2014).

[46] M. Calciati, A. Tibaldi, F. Bertazzi, M. Goano, and P. Debernardi, Many-valley electron transport in AlGaAs VCSELs, Semiconductor Sci. Technol. **32**, 055007 (2017).

[47] H. T. Luo, W. Z. Shen, Y. H. Zhang, and H. F. Yang, Study of band gap narrowing effect in n-GaAs for the application of far-infrared detection, Phys. B **324**, 379 (2002).

[48] Ioffe Physico-Technical Institute, Physical properties of semiconductors, St. Petersburg, Russia.

[49] C. Rivas, R. Lake, G. Klimeck, W. R. Frensley, M. V. Fischetti, P. E. Thompson, S. L. Rommel, and P. R. Berger, Full-band simulation of indirect phonon assisted tunneling in a silicon tunnel diode with delta-doped contacts, Appl. Phys. Lett. **78**, 814 (2001).

[50] W. Vandenberghe, B. Sorée, W. Magnus, and M. V. Fischetti, Generalized phonon assisted Zener tunneling in indirect semiconductors with non-uniform electric fields: A rigorous approach, J. Appl. Phys. **109**, 124503 (2011).

[51] J. Chen, and J. Gong, Theoretical investigation of the phonon-assisted tunneling in TFET with an indirect band gap semiconductor, Superlatt. Microstruct. **111**, 319 (2017).

[52] M. Luisier, and G. Klimeck, Simulation of nanowire tunneling transistors: From the Wentzel-Kramers-Brillouin approximation to full-band phonon-assisted tunneling, J. Appl. Phys. **107**, 084507 (2010).

[53] M. Mohammed, A. S. Verhulst, D. Verreck, M. L. Van de Put, W. Magnus, B. Sorée, and G. Groeseneken, Phonon-assisted tunneling in direct-bandgap semiconductors, J. Appl. Phys. **125**, 015701 (2019).

[54] C. D. Bessire, M. T. Björk, H. Schmid, A. Schenk, K. B. Reuter, and H. Riel, Trap-assisted tunneling in Si-InAs nanowire heterojunction tunnel diodes, Nano Lett. **11**, 4195 (2011).

[55] G. Kolhatkar, J. F. Wheeldon, C. E. Valdivia, A. W. Walker, S. Fafard, A. Turala, A. Jaouad, R. Arès, V. Aimez, and K. Hinzer, in *SPIE Photonics North (2010), Proceedings*

of the SPIE Vol. 7750 (SPIE digital library, Niagara Falls, Canada, 2010), p. 77502S.

[56] M. G. Pala, C. Grillet, J. Cao, D. Logoteta, A. Cresti, and D. Esseni, Impact of inelastic phonon scattering in the OFF state of tunnel-field-effect transistors, J. Comp. Electron. **15**, 1240 (2016).

[57] M. Mandurrino, G. Verzellesi, M. Goano, M. Vallone, F. Bertazzi, G. Ghione, M. Meneghini, G. Meneghesso, and E. Zanoni, Physics-based modeling and experimental implications of trap-assisted tunneling in InGaN/GaN light-emitting diodes, Phys. Status Solidi A **212**, 947 (2015).

[58] U. Aeberhard, Nonequilibrium Green's function picture of nonradiative recombination of the Shockley-Read-Hall type, Phys. Rev. B **99**, 125302 (2019).

[59] G. Verzellesi, D. Saguatti, M. Meneghini, F. Bertazzi, M. Goano, G. Meneghesso, and E. Zanoni, Efficiency droop in InGaN/GaN blue light-emitting diodes: Physical mechanisms and remedies, J. Appl. Phys. **114**, 071101 (2013).

[60] Y.-A. Chang, T.-S. Ko, J.-R. Chen, F.-I. Lai, C.-L. Yu, I.-T. Wu, H.-C. Kuo, Y.-K. Kuo, L.-W. Laih, L.-H. Laih, T.-C. Lu, and S.-C. Wang, The carrier blocking effect on 850 nm InAlGaAs/AlGaAs vertical-cavity surface-emitting lasers, Semiconductor Sci. Technol. **21**, 1488 (2006).

[61] M. Meneghini, C. De Santi, A. Tibaldi, M. Vallone, F. Bertazzi, G. Meneghesso, E. Zanoni, and M. Goano, Thermal droop in III-nitride based light-emitting diodes: Physical origin and perspectives, J. Appl. Phys. **127**, 211102 (2020).

[62] P. Enders, A. Bärwolff, M. Woerner, and D. Suisky, $\mathbf{k}\cdot\mathbf{p}$ theory of energy bands, wave functions, and optical selection rules in strained tetrahedral semiconductors, Phys. Rev. B **51**, 16695 (1995).

[63] R. G. Veprek, S. Steiger, and B. Witzigmann, Ellipticity and the spurious solution problem of $k\cdot p$ envelope equations, Phys. Rev. B **76**, 165320 (2007).

[64] D. L. Smith, and C. Mailhiot, Theory of semiconductor superlattice electronic structure, Rev. Modern Phys. **62**, 173 (1990).

[65] M. Luisier, A. Schenk, W. Fichtner, and G. Klimeck, Atomistic simulation of nanowires in the $sp^3d^5s^*$ tight-binding formalism: From boundary conditions to strain calculations, Phys. Rev. B **74**, 205323 (2006).